3D analysis of dissection photographs with surface scanning and machine learning for quantitative neuropathology

Harshvardhan Gazula[a], Henry F. J. Tregidgo[b], Benjamin Billot[c], Yael Balbastre[a], Jonathan William-Ramirez[a], Rogeny Herisse[a], Adrià Casamitjana[b,d], Erica J. Melief[e], Caitlin S. Latimer[e], Mitchell D. Kilgore[e], Mark Montine[e], Eleanor Robinson[b], Emily Blackburn[b], Michael S. Marshall[f], Theresa R. Connors[f], Derek H. Oakley[f], Matthew P. Frosch[f], Koen Van Leemput[a,g], Adrian V. Dalca[a,c], Bruce Fischl[a], Christine L. Mac Donald[h], C. Dirk Keene[e], Bradley T. Hyman[f], and Juan Eugenio Iglesias[a,b,c,1]

This manuscript was compiled on June 7, 2023

Dissection photographs are routinely acquired in brain banks but seldom used for quantitative analysis. We present a publicly available, open-source toolbox of computational methods for 3D analysis of photographs of dissected slices of human brains. The toolbox includes methods for: *(i)* Geometric preprocessing of the photographs; *(ii)* 3D volumetric reconstruction of a human brain or hemisphere from the photographs and, optionally, a surface scan; and *(iii)* automatic 3D segmentation of nine bilateral brain regions using a novel machine learning method ("Photo-SynthSeg"), which is capable of "interpolating" the 3D segmentation across the gaps between photographs with large spacing in between. Our tools can be used for quantitative brain analysis at the macroscopic level (e.g., volumetry), as a substitute for *ex vivo* magnetic resonance imaging (MRI) – which requires access to an MRI scanner and *ex vivo* scanning expertise. Our tools are also helpful for computationally guided dissection of brain areas that are difficult to identify from the slices, e.g., defined by functional atlases. Finally, our tools also provide a spatial mapping between the a 3D MRI scan (when available) and the 2D slices, which enables accurate neuropathological-neuroimaging correlation. We evaluate our toolbox on a synthetic dataset and on dissection photographs from two NIH Alzheimer's Disease Research Centers (ADRC). Our methodology yields accurate 3D reconstruction and automated segmentations that are highly correlated to those obtained from *ex vivo* MRI, and that can detect expected differences between brains with Alzheimer's disease and controls. The tools are available as part of our widespread neuroimaging suite "FreeSurfer" (https://surfer.nmr.mgh.harvard.edu/fswiki/PhotoTools).

3D scanning | 3D reconstruction | segmentation | dissection photography | neuropathology to neuroimaging correlation

Significance Statement

When donated human brains are dissected at brain banks, they are first cut into slabs that are routinely photographed just with archiving purposes. Here we present a set of novel, open-source computational tools that enable 3D reconstruction of these photographs into a volumetric dataset, as well as subsequent 3D segmentation of the reconstructed volumes (i.e., assigning neuroanatomical labels to every pixel in the images). Our tools enable quantitative analyses of the brain at the macroscopic level (e.g., measuring volumes of brain regions) without requiring MRI scans of the specimens. The tools also provide a spatial mapping between an MRI (if available) and the photographs, thus enabling the study of correlations between macroscopic and microscopic features (e.g., atrophy vs histology).

DRAFT

Morphometric measurements such as cortical thickness and subcortical volumetry can be used as surrogate biomarkers of aging (1–3) and disease (4–7) via confirmed histopathological changes. Integrating neuroimaging tools with the neuropathological assessment can enable neuropathological-neuroimaging correlations for studying neurodegenerative diseases, i.e., connecting macroscopic imaging with histological ground truth derived from microscopic imaging (8). While *ante mortem* MRI studies provide accurate and reliable morphometric data, they are often unavailable or occur too long before death, impeding reliable histopathological correlation. Cadaveric MRI can circumvent these challenges, but logistic and legal issues often complicate this procedure.

An alternative to cadaveric imaging is *ex vivo* MRI, which enables high-resolution image acquisition free of subject motion and other physiological noise (9). *Ex vivo* MRI also has disadvantages, including: tissue degradation due to bacteria and autolysis from death to initiation of tissue fixation; cross-linking of proteins due to fixation that dramatically changes MR properties of the tissue; and image artifacts caused by magnetic susceptibility interfaces that do not occur *in vivo* (10).

Ex vivo MRI is relatively uncommon in brain banks that seek to establish neuropathological-neuroimaging correlations (11, 12). However, dissection photography is routine in nearly every brain bank: the specimens they collect are typically dissected into coronal slices and photographed before further blocking and histological analysis. These photographs, often underutilized, are an invaluable information resource that, if leveraged appropriately, can play a vital role in advancing our understanding of various brain functions and disorders — mainly when *ex vivo* MRI is unavailable. To this end, we propose a novel software suite that,

Author affiliations: [a]Martinos Center for Biomedical Imaging, MGH and Harvard Medical School, Charlestown, MA; [b]Centre for Medical Image Computing, University College London, London, UK; [c]Computer Science and Artificial Intelligence Laboratory, MIT, MA, USA; [d]Biomedical Imaging Group, Universitat Politècnica de Catalunya, Spain; [e]Laboratory Medicine and Pathology, UW School of Medicine, WA, USA; [f]Massachusetts Alzheimer Disease Research Center, MGH and Harvard Medical School, Charlestown, MA; [g]Neuroscience and Biomedical Engineering, Aalto University, Espoo, Finland; [h]Neurological Surgery, UW School of Medicine, WA, USA

Conceptualization: HG, HFJT, AC, BB, BF, JEI. Methodology: HG, HFJT, BB, YB, AC, KVL, AVD, BF, JEI. Software: HG, HFJT, BB, AC, JEI. Investigation: HG, HFJT, BB, JWR, RH, EJM, CSL, MDK, ER, EB, MSM, DHO, MPF, JEI. Resources: MPF, BF, CLM, DCK, BTH. Data curation: JWR, RH, EJM, CSL, MDK, ER, EB, MSS, DHO. Visualization: HG, JWR, RH, YB, JEI. Writing (original draft): HG, JEI. Writing (review and editing): All authors. Labelers: ER, EB.

BF has a financial interest in CorticoMetrics, a company developing brain MRI measurement technology. His interests are reviewed and managed by MGH.

[1]Corresponding author: jiglesiasgonzalez@mgh.harvard.edu

for the first time, enables 3D reconstruction and quantitative 3D morphometry of dissection photographs, powered by modern machine learning techniques (13) and 3D surface scanning (14). Specifically, our tools enable volumetric analysis of brain structures from the photographs, computationally guided dissection via automated segmentation, and accurate spatial mapping for neuropathological-neuroimaging correlation.

Our suite is freely available and includes three modules. The first module is a set of preprocessing routines for the photographs that enables the correction of perspective and calibration of pixel sizes. The second module is a joint image registration algorithm that allows 3D reconstruction of the photographs using a 3D surface scan of the brain as a reference. This module can also use a probabilistic atlas as a reference for the reconstruction circumventing the need for a surface scanner. This mode enables retrospective analysis of photographs without corresponding 3D scans, albeit with lower accuracy than if surface scanning was available. The third and final module uses machine learning to provide a volumetric image segmentation of the 3D reconstructed stack. This module combines a state-of-the-art deep segmentation neural network (a U-Net (15)) with a domain randomization approach (16), thus enabling analysis of photographs with different intensity profiles, e.g., acquired under various illumination conditions, with different cameras or camera settings, or from fixed or fresh tissue. Moreover, the machine learning method enables the estimation of "smooth", isotropic segmentations that accurately interpolate across the gaps between the coronal planes captured in the photographs.

This article extends our previous work (17) by *(i)* improving upon the 3D reconstruction methods; *(ii)* using machine learning (rather than Bayesian methods) to produce segmentations that are more accurate and also isotropic (i.e., provide labels in between slices); and *(iii)* providing extensive experiments on different synthetic and real datasets.

The rest of this article is organized as follows. In Section 1, we elaborate on the technicalities of the preprocessing steps, the reconstruction algorithm, and the deep learning segmentation method. A detailed description of the datasets, experiments, and accompanying results is provided in Section 2. Section 3 discusses the results and Section 4 concludes the article.

1. Methods

This section describes the methods for data acquisition, preprocessing, reconstruction, and segmentation. The workflow is summarized in Figure 1 and comprises: sample preparation (Figure 1A); surface scanning (Figure 1B); specimen slicing and photography (Figure 1C); preprocessing of photographs (Figure 1D); 3D reconstruction (Figure 1E); and 3D segmentation at 1 mm isotropic resolution (Figure 1F).

A. Surface scanning. Surface scanning (also known as "profilometry") is a technology that is becoming increasingly inexpensive (a few thousand dollars), mainly via structured light technology (14). The preferred version of our proposed pipeline relies on a surface scan of the specimen (Figure 1A) acquired before slicing. This surface scan, represented by a triangular mesh, is used as an external reference to guide the 3D reconstruction of the photographs (details in Section D below).

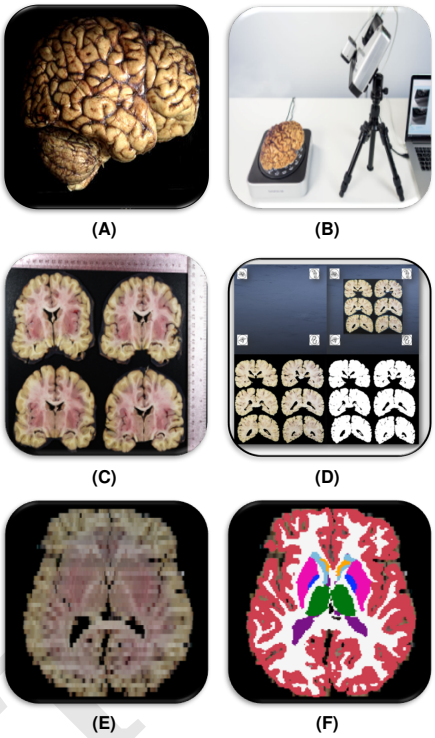

Fig. 1. Proposed pipeline. **(A)** Specimen (fixed or fresh). **(B)** Surface scan acquisition. **(C)** Tissue slicing and photography. **(D)** Preprocessing of photographs to calibrate pixel size and correct perspective. **(E)** 3D volumetric reconstruction using surface scan as reference. **(F)** Segmentation using proposed method ("PhotoSynthSeg").

While there are no specific technical requirements for this scan (e.g., minimum resolution), minimizing geometric distortion (i.e., deformation) between scanning and subsequent slicing is crucial. The surface scan may be acquired with a handheld scanner with the specimen placed on a table, or with the scanner on a triped and the sample on a turntable. An example of an acquisition setup and a sample surface scan are shown in Figure 2. As mentioned earlier, our pipeline does not strictly require the surface scan, as it can be replaced with a probabilistic atlas with a slight loss of accuracy (see Section D below).

B. Tissue slicing and photography. In preparation for the downstream 3D reconstruction, some requirements exist for the dissection and photography of the brain slabs. Specifically, our pipeline assumes that parallel slices of approximately constant thickness are cut in (approximately) coronal direction – which is the standard practice in brain banks. Moreover, we require the presence of fiducials to enable pixel size calibration and perspective correction. Ideally, four fiducials are placed on the corners of a rectangle of known dimensions (Figure 3A). In the absence of such fiducials, we require the presence of at least a ruler or two orthogonal rulers; the former enables pixel size calibration via image scaling, whereas the latter enables approximate perspective correction by fitting an affine transform.

Our pipeline allows for multiple slices to be present in one photograph but requires that all photographs are of the same side of the slices (either anterior or posterior) and that the

DRAFT

(A)

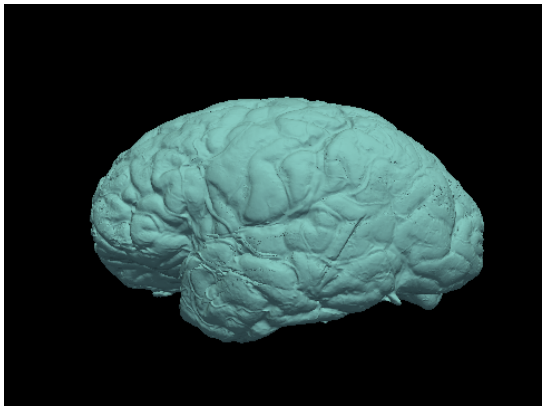

(B)

Fig. 2. Surface scanning. (A) Sample equipment setup using a tripod and a turntable; scans acquired with handheld devices are also compatible with our tools. **(B)** Surface scan of a left hemisphere, represented as a triangular mesh.

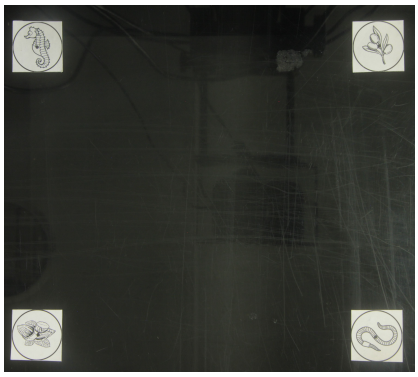

(A)

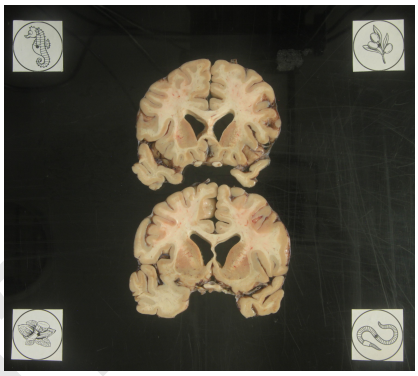

(B)

Fig. 3. Photography setup. (A) Image of the board (with fiducials placed in the corners) before photographing tissue. This image will be used as a template to correct and calibrate subsequent photographs with tissue slices. **(B)** Photograph or two coronal slices simultaneously on the same board.

inferior-superior direction of the anatomy is approximately aligned with the vertical axis of the image (as in Figure 3B). Additionally, the slices should ideally be photographed on a flat board with a solid background color that stands out from the brain tissue, as stronger contrast between tissue and background greatly facilitates image segmentation when preprocessing the photographs (see Section C below).

C. Preprocessing of photographs. Image preprocessing starts with geometric correction, i.e., pixel size calibration and perspective correction. In the ideal scenario, our software is first calibrated with a photograph of the board with just the fiducials and no brain tissue (Figure 3A), for which the user specifies the centers of the fiducials (by clicking on them) and the distances between them (in mm). When a new "test" image (Figure 3B) with brain tissue is fed to the software, our tools use the widespread scale-invariant feature transform (SIFT (18)) to detect (Figure 4A, 4B) and match (Figure 4C) keypoints between the reference and test images. Crucially, the keypoint detection is limited to four circular regions around the fiducials in the reference image. This operation enables the software to map the fiducial locations from the reference image to the test photograph. Given the (x, y) coordinates of the fiducials, we use a least squares fitting procedure to fit a perspective transform (Figure 4D) that maps these coordinates to the corners of the rectangle in physical coordinates: $(0, 0)$, $(W, 0)$, $(0, H)$, and (W, H), where W and H are the width and height of the rectangle in mm. This transform is finally used to resample the photographs to a space of predefined pixel dimensions (in practice, we use 0.1 mm), which is perfectly aligned to the rectangle (Figure 4E). A digital ruler is also added to the corrected image (Figure 4E).

Our software also supports a manual mode where the user clicks on the corners of the rectangle in every image. This is useful when no fiducials are present, but the user can still identify the corners of a rectangle of known dimensions in the image, e.g., if the board has an imprinted grid pattern. The software also supports geometric correction with two or three manually placed landmarks. The former is useful when only a ruler is present on the image and enables coarse pixel size correction by scaling the image proportionally to the length of the ruler (provided by the user). The latter is useful when two orthogonal rulers are present; while fitting a perspective transform requires four points, one can still perform approximate perspective correction by fitting an affine transform – which only requires three points.

After geometric correction, our methods require a binary segmentation of the brain tissue, separating it from the background (Figure 5A). If a solid background is used, this can be achieved simply by thresholding the image intensities; otherwise, manual intervention may be needed. Given this binary mask, the final preprocessing step requires the user to specify the order of the slices within the photograph – which may be anterior to posterior or vice versa, but must be consistent within and across photographs of the same case. Moreover, the user also needs to specify whether two connected components belong to the same slice, which often

DRAFT

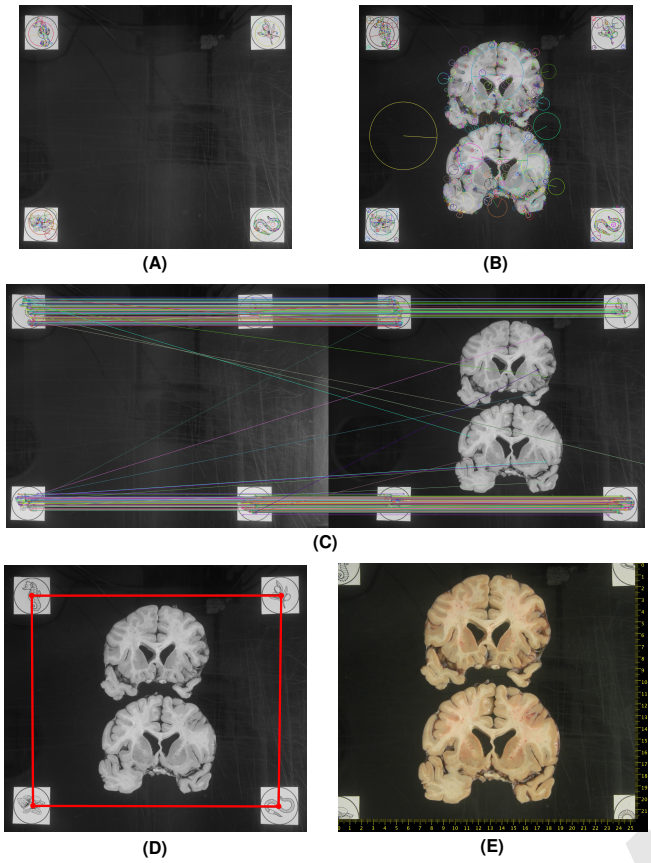

Fig. 4. Photograph preprocessing. (A) Keypoints detected in the calibration template using SIFT; we note that SIFT operates on grayscale images. **(B)** Keypoints in a "test" image with tissue. **(C)** Matching keypoints. **(D)** Automatic identification of fiducials on corners. **(E)** Final image corrected for perspective and calibrated for pixel size, with a digital ruler included.

happens around the temporal pole. This can be accomplished with a dedicated graphical user interface that we distribute with our tools (Figure 5B).

D. 3D volumetric reconstruction from photographs. Recovering a 3D volume from a stack of 2D images entails a consistent 3D reconstruction of the stack via joint image alignment – known as "registration" (19–22). We pose 3D reconstruction as a joint optimization problem (23, 24) and use a 3D reference volume for the registration. This volume is ideally a binary 3D mask (Figure 6A) obtained by rasterizing ("filling") the triangular mesh from the surface scan. If a surface scan is not available, one can instead use a probabilistic atlas (25) of brain shape (Figure 6B), which provides a rough reference for the reconstruction. However, this reference cannot drive the reconstruction toward the actual shape of the specimen nor correct deviations from the user-provided slice thickness.

Given N photographed slices and their corresponding masks, the goal of this optimization framework is to simultaneously identify: *(i)* a set of N 2D affine geometric transforms $\{\phi_n\}_{n=1,\ldots,N}$ (rotation, translation, shear, and scaling for each slice); *(ii)* a scaling factor s in the anterior-posterior direction shared by all slices; and *(iii)* a rigid 3D transform Ψ for the reference (rotation and translation). These transforms seek to align the slices with each other and with the reference volume. We note that affine transforms (rather than rigid)

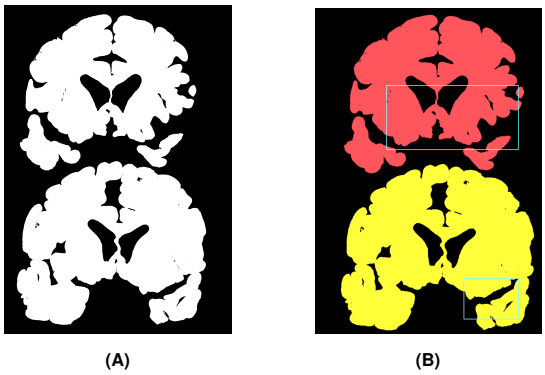

Fig. 5. Photograph preprocessing (continued). (A) Segmentation of brain tissue and background; note that using a solid black background enables segmentation by simple thresholding. **(B)** User defined rectangles to specify order of slices and grouping of disconnected portions of tissue into slabs.

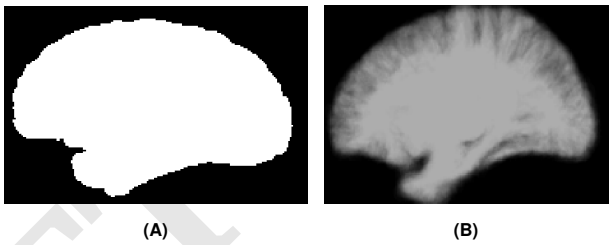

Fig. 6. Sample volumetric references for 3D reconstruction. (A) Sagittal slice of binary 3D volume obtained by rasterizing ("filling") the triangular mesh from the surface scan. **(B)** Comparable slice of probabilistic atlas (we use the LPBA40 atlas (25)).

are required for the photographs due to imperfections in the image preprocessing of the previous section; nevertheless, we expect the shear and scaling of these transforms to be small. Similarly, the scaling s in the anterior-posterior direction is required to correct deviations from the slice thickness specified by the user, which is never exact.

The optimal set of transforms is obtained by maximizing the objective function $\mathcal{F}$ in Equation 1. This objective encodes four desired attributes of the reconstructed data:

1. A high overlap between the stack of N 3D reconstructed slice masks $M\left[\boldsymbol{x};\{\Phi_n\},s\right]$ and the aligned reference volume $R[\boldsymbol{x};\Psi]$. We note that images are a function of spatial location $\boldsymbol{x}$.

2. A high similarity between the image intensities of successive (reconstructed) slices $S_n\left[\boldsymbol{x};\Phi_n,s\right]$ and $S_{n+1}\left[\boldsymbol{x};\Phi_{n+1},s\right]$, for $n=1,\ldots,N-1$.

3. A high overlap between successive (reconstructed) slice masks $M_n\left[\boldsymbol{x};\Phi_n,s\right]$ and $M_{n+1}\left[\boldsymbol{x};\Phi_{n+1},s\right]$, for $n=1,\ldots,N-1$.

4. Minimal scaling and shear in the 2D affine transforms; the function f is a regularizer that prevents excessive deformation of the slices – particularly those showing little tissue, e.g., the first and last slices of the stack.

To allow an equation to span both columns, use the `\begin{figure*}...\end{figure*}` environment mentioned above for figures.

Note that the use of the `widetext` environment for equations is not recommended, and should not be used.

DRAFT

$$\mathcal{F}\left(\Psi,\{\Phi_n\}\right) = \underbrace{\alpha\mathcal{D}\left(M\left[\boldsymbol{x};\{\Phi_n\},s\right],R[\boldsymbol{x};\Psi]\right)}_{\text{1) volume-to-volume mask overlap}} + \underbrace{\beta\frac{1}{N-1}\sum_{n=1}^{N-1}\mathcal{C}\left(S_n\left[\boldsymbol{x};\Phi_n,s\right],S_{n+1}\left[\boldsymbol{x};\Phi_{n+1},s\right]\right)}_{\text{2) slice-to-slice cross-correlation}}$$
$$+ \underbrace{\gamma\frac{1}{N-1}\sum_{n=1}^{N-1}\mathcal{D}\left(M_n\left[\boldsymbol{x};\Phi_n,s\right],M_{n+1}\left[\boldsymbol{x};\Phi_{n+1},s\right]\right)}_{\text{3) slice-to-slice mask overlap}} - \underbrace{\nu\frac{1}{N}\sum_{n=1}^{N}f\left(\Phi_n\right)}_{\text{4) regularizer}} \quad [1]$$

Mathematically, overlap in Equation 1 is measured with the soft Dice coefficient $\mathcal{D}$ (26–28); image similarity is measured with the normalized cross-correlation $\mathcal{C}$; and the scaling and shearing are measured with the absolute value of the logarithm of the determinant of the affine matrices, i.e., $f\left(\Phi_n\right)$ is the absolute log-determinant of the 3×3 matrix encoding Φ_n. The constants α,β,γ,ν are relative weights. The objective function $\mathcal{F}$ is minimized with standard numerical methods – specifically the LBFGS algorithm (29). The LBFGS optimizer is initialized by stacking the photographs with their centers of gravity on coordinate $(0,0)$, and then matching the center of gravity of the whole stack with the center of gravity of the 3D reference.

If a probabilistic atlas is used instead of the surface scan, the same objective function is used but with a slightly different search space. Since we can no longer trust the external reference to correct for fine shape correction: *(i)* we keep the scaling factor of the anterior-posterior direction fixed to $s=1$ (i.e., we trust the slice thickness specified by the user); *(ii)* we use rigid rather than affine transforms $\{\phi_n\}$ for the slices (which also has the effect of making the regularizer equal to zero); and *(iii)* we use a full 3D affine transform Ψ for the reference.

Sample reconstructions of a case with 3D surfaces and probabilistic atlases are shown in Figures 7A and 7B, respectively. Further examples are shown in Figure S1 in the supplement.

E. Segmentation. The 3D reconstructed photographs have various applications (e.g., volumetry, computationally guided dissection) which require image segmentation, i.e., assigning neuroanatomical labels to every spatial location (30–32). There are two main challenges when segmenting the 3D reconstructed photographs. First, the appearance of the images varies widely across cases due to differences in camera hardware (sensor, lens), camera settings, illumination conditions, and tissue preparation (e.g., fixed versus fresh). And second, accurate volumetry requires estimating the segmentation not only on the planes of the photographs but also in between slices.

In our previous work (17), we adopted a Bayesian segmentation strategy that handled the first issue but not the second. Here, we extend a machine learning approach based on domain randomization (33) that we have successfully applied to segment clinical brain MRI scans with large slice spacing (34, 35). Specifically, our newly proposed approach "Photo-SynthSeg" trains a convolutional neural network for image segmentation (a 3D U-Net (15, 36)) with synthetic data as follows.

"Photo-SynthSeg" starts from a training dataset that comprises a pool of 3D segmentations of brain images at isotropic 3D resolution (Figure 8A). At every iteration during training, one of these 3D segmentations is randomly selected and geometrically deformed with a random nonlinear transform, which simulates imperfect 3D reconstruction by including a "deformation jitter" in the coronal direction, i.e., small but abrupt deformations from one coronal slice to the next (Figure 8B). This deformed isotropic segmentation is used to generate a synthetic 3D image (also at isotropic resolution) using a Gaussian mixture model conditioned on the segmentation (Figure 8C). Crucially, we randomize the Gaussian parameters (means and variances) to make the neural network robust against variations in image appearance. This synthetic isotropic image is then "digitally sliced" into a 3D stack of synthetic coronal photographs, each of which is independently corrupted by a random 2D smooth illumination field that simulates inhomogeneities in the illumination of the photographs (Figure 8D). Importantly, we also randomize the thickness of the simulated slices in every iteration and introduce small stochastic variations in thickness around the central value within each simulation. This strategy makes the network agnostic to the slice thickness of the reconstructed 3D stack at test time. Finally, the simulated stack, which has anisotropic resolution (e.g., 1mm in-plane and several mm in slice thickness), is resampled to the original isotropic resolution of the (deformed) 3D segmentation (Figure 8E).

This generative process mimics the image formation process in the real world and has two crucial aspects. First, domain randomization: sampling different Gaussian parameters, illumination fields, and slice thicknesses at every iteration beyond realistic limits (as in Figure 8, where even contralateral regions have different appearance) forces the U-Net to learn features that are independent of the intensity profiles of the photographs, as well as of the spacing between slices. This process makes the U-Net robust against changes in the acquisition. And second, the super-resolution component: Photo-SynthSeg is a U-Net that will produce a high-resolution (1 mm) isotropic 3D segmentation for every input at test time, independently of the slice spacing of the 3D reconstructed stack of photographs (Figure 9).

During training, resampled stacks and corresponding segmentations (Figure 8B-8E) are fed to the U-Net. The U-Net architecture is the same as in our previous works with synthetic scans (16, 34, 37): it consists of five levels, each separated by a batch normalization layer (38) along with a max-pooling (contracting path) or an upsampling operation (expanding path). All levels comprise two convolution layers with $3\times3\times3$ kernels. Every convolutional layer is associated with an Exponential Linear Unit activation (39), except for the last one, which uses a softmax. While the first layer comprises 24 feature maps, this number is doubled after each max-pooling, and halved after each upsampling. Following the original U-Net architecture, skip connections are used

DRAFT

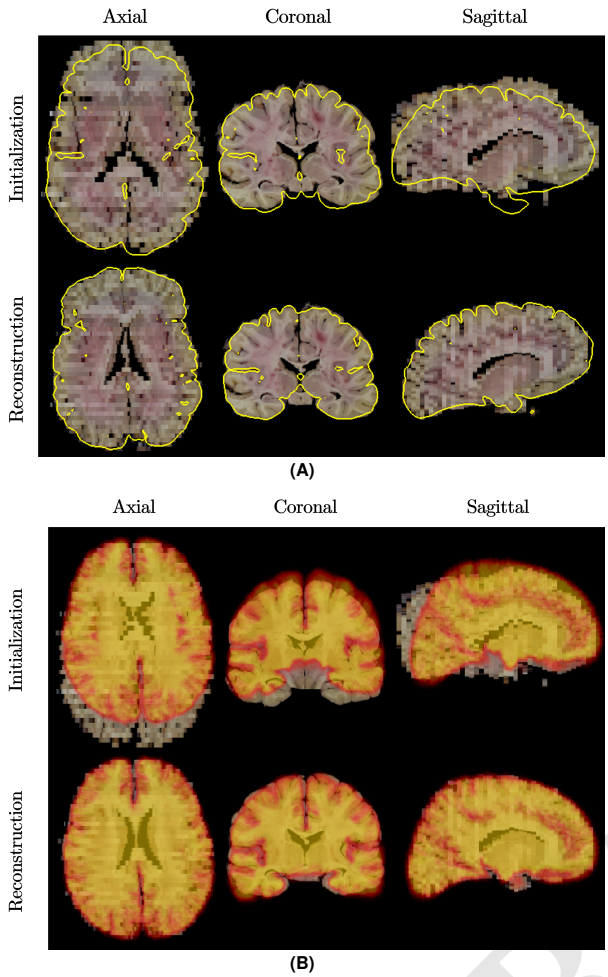

Fig. 7. 3D reconstruction from dissection photographs. (A) Axial, coronal, and sagittal views of the photograph stack at initialization and after reconstruction. The reference surface is marked as a yellow line. **(B)** Save views when reconstructing witha probabilistic atlas (overlaid as a transparent heat map). Note that the reconstruction with a probabilistic atlas is plausible, but with a shape that is biased towards the atlas.

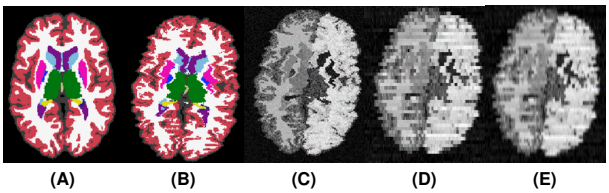

Fig. 8. Intermediate steps in the generative process. (A) Randomly sampled input label map from the training set. **(B)** Spatially augmented input label map; imperfect 3D reconstruction is simulated with a deformation jitter across the coronal plane. **(C)** Synthetic image obtained by sampling from a Gaussian Mixture Model conditioned on the segmentation, with randomized means and variances. **(D)** Slice spacing is simulated by downsampling to low resolution. This imaging volume is further augmented with a bias field and intensity transforms (brightness, contrast, gamma). **(E)** The final training image is obtained by resampling (D) to high resolution. The neural network is trained with pairs of images like E (input) and B (target).

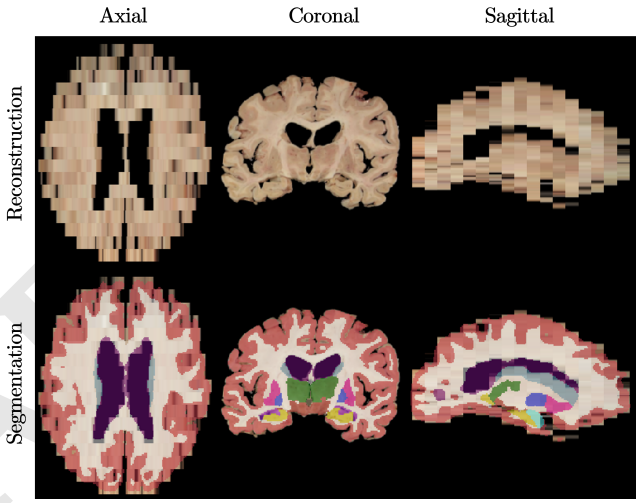

Fig. 9. Photo-SynthSeg. Axial, coronal, and sagittal views of the reconstruction and segmentation of a sample whole cerebrum. Please note that the segmentations have an isotropic resolution of 1 mm – despite the larger slice spacing, which is approximately 10 mm.

across the contracting and expanding paths. The network is trained with a soft Dice loss (28) and the Adam optimizer (40). The deep learning model is implemented in Keras (41) with a Tensorflow backend (42). Training takes around seven days on a Nvidia Quadro RTX 6000 graphics processing unit (GPU).

2. Experiments and Results

This section describes experiments to quantitatively evaluate the accuracy of our 3D reconstruction and segmentation procedures using a combination of real and synthetic datasets.

A. Datasets. T1-39: 39 T1-weighted MRI scans at 1 mm isotropic resolution, with manual volumetric segmentations for 36 brain structures. We use these volumetric segmentations to train Photo-SynthSeg. This is the labeled dataset used to build the probabilistic atlas in FreeSurfer. Further details on the dataset can be found in (43).

HCP: T1- and T2-weighted MRI scans of 500 subjects from the Human Connectome Project, acquired at 0.7 mm isotropic resolution. The scans were skull stripped using Freesurfer (44). We use these scans to simulate dissection photographs and matching surface scans by digitally slicing the T2 scans and using the T1 as a 3D reference to reconstruct the T2 slices (details in Section B). Further details on the MRI acquisition can be found in (45).

UW-ADRC: Dissection photography of fixed tissue and companion *ex vivo* MRI scans for 24 cases (all of them with both hemispheres) from the ADRC at the University of Washington. The MRI scans were acquired at 0.8 mm isotropic resolution using a FLAIR sequence. Coronal slices were cut with 4 mm thickness using a modified deli slicer and photographed with a 35 Megapixel (MP) camera. This dataset enables us to compute volumetric measurements from the 3D reconstructed photographs and compare them with reference values obtained from the corresponding MRI scans (i.e., a silver standard). Furthermore, two experienced labelers manually traced the contour of 9 brain regions (white matter, cortex, lateral ventricle, thalamus, caudate, putamen, pallidum, hippocampus, and amygdala) in one slice per case, which enables computation of Dice scores. Further details on the dissection and processing of the specimens can be found in Appendix A and (46).

DRAFT

MADRC: Dissection photography of fixed tissue and companion surface scans for 78 cases from the Massachusetts ADRC (18 whole cerebrums and 58 hemispheres). The surface scans were acquired using a turntable with an Einscan Pro HD scanner (Shining 3D, Hangzhou, China, 0.05 mm point accuracy). Slices with variable thickness were cut with a dissecting knife on a predefined set of landmarks and photographed with a 15.1 MP Canon EOS 50D Digital SLR camera. This dataset enables evaluation of our methods in a challenging real-world scenario with tissue cut into thick, uneven slices (∼10 mm thick). Further details on the dissection and processing of the specimens can be found in Appendix B.

B. Quantitative evaluation of reconstruction with digitally sliced MRI data. In this experiment, we assess the fidelity of the 3D reconstruction algorithm by measuring the registration error (in mm). Measuring such errors with real data would require manual annotation of pairs of matching landmarks, which is labor-intensive, error-prone, and not reproducible. Instead, we use simulated (digitally sliced) data created from MRI scans. While the measured errors are optimistic compared with real sliced tissue, this approach enables us to estimate the error as a continuous function of slice thickness without manual annotation effort.

For this purpose, we used the HCP dataset, letting the T1 and T2 scans play the role of 3D reference and dissection photographs, respectively, as follows. To simulate dissection photographs of slices with $S \times 0.7$ mm thickness ($S = 2, 4, 8, 16$), we: extracted one coronal slice every S from the T2 scan; applied a random affine transform to each slice; and added a random illumination field to each deformed slice to simulate variations in illumination at the time of photography. This simulation procedure is illustrated in Figure S2 in the supplement. Then, we used the algorithm in Section D to 3D reconstruct the slices into their original shape, using the (isotropic) 3D mask of the T1 scan (with a random rigid transform applied) as a reference. The registration error was calculated as the mean voxel displacement in mm between the reconstructed and ground truth T2 slices. Additionally, to test the robustness of the reconstruction algorithm to uneven slice spacing during dissection, we also analyze the error when a random variation of the nominal thickness ("thickness jitter") is introduced for every slice.

Figure 10 shows the box plot for the mean reconstruction error as a function of the slice spacing and thickness jitter. The results show that the reconstruction error is reasonably robust to increased slice spacing. On the other hand, thickness jitter yields greater increases in reconstruction error, particularly at larger slice spacings. This result highlights the importance of keeping the slice thickness as constant as possible during acquisition.

C. Quantitative evaluation of segmentation with Photo-SynthSeg. To assess the accuracy of Photo-SynthSeg, we 3D reconstructed the brain volumes from the photographs of the 24 UW-ADRC cases using the methodology described in Section D. The reference volume is a binarized mask derived from the subjects' MRI scans. Following this step, the 3D reconstructions are automatically segmented using Photo-SynthSeg, and compared with the ground truth. We compare the results against our previously presented segmentation method "SAMSEG". SAMSEG is a segmentation method originally conceived for brain MRI (47), which employs Bayesian techniques to segment MRI scans irrespective of their contrast and pulse sequence. As we showed in (17), this technique can be adapted to segment 3D reconstructed photographs. Sample segmentations with the two methods are shown in Figure 11.

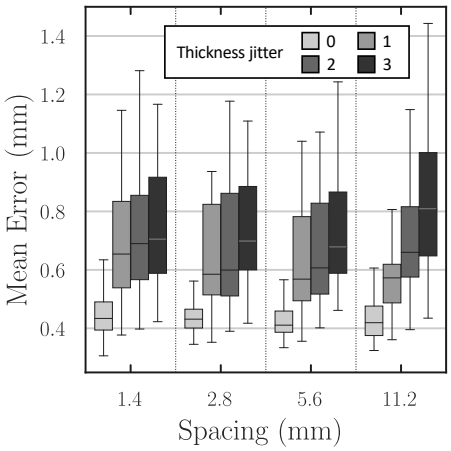

Fig. 10. Reconstruction error (in mm) in synthetically sliced HCP data. Box plots for the mean reconstruction error as a function of spacing and thickness jitter. A jitter of j means that the nth slice is extracted from the interval $[n-j, n+j]$ (rather than exactly n). The center of each box represents the median; the edges of the box represent the first and third quartile; and the whiskers extend to the most extreme data points not considered outliers (not shown, in order not to clutter the plot.

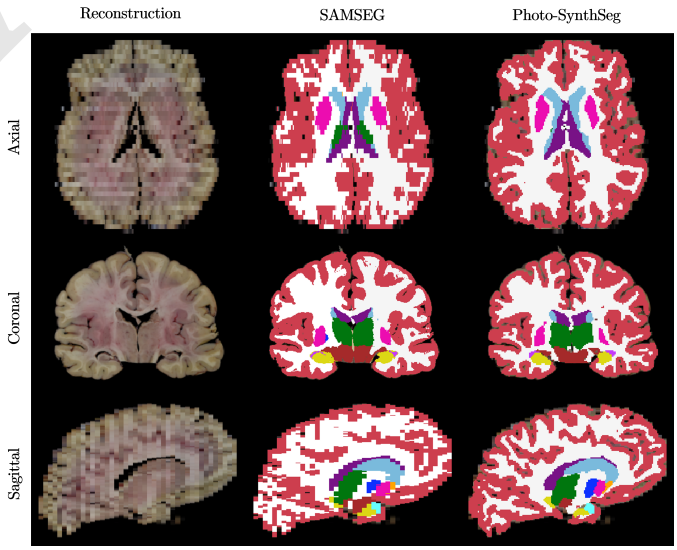

Fig. 11. Comparison of SAMSEG vs Photo-SynthSeg. Axial, coronal, and sagittal views of the reconstruction and automated segmentation of a sample whole brain from the UW-ADRC dataset, using SAMSEG and Photo-SynthSeg.

We first evaluate Photo-SynthSeg and SAMSEG *directly*, with Dice scores computed against the manual segmentations available on a single selected slice per subject (Figure 12). The figure also shows two ablations: using a probabilistic atlas instead of the mask derived from the MRI; and training Photo-SynthSeg with a fixed 4 mm spacing instead of randomizing

DRAFT

the spacing during training. The former enables us to assess the impact of having a case-specific 3D reference available, whereas the latter enables evaluating the effectiveness of the thickness randomization strategy. The results show that Photo-SynthSeg outperforms SAMSEG, producing Dice scores over 0.8 for all structures except the amygdala. The plots also show that using the probabilistic atlas produces realistic enough reconstructions, such that the 2D Dice scores remain high. Finally, the results also show the superiority of the thickness randomization strategy over the fixed spacing strategy, even if the latter had access to the ground truth spacing of the photographs. This is consistent with our previous findings in MRI segmentation, where domain randomization strategies also outperformed targeted simulations (37).

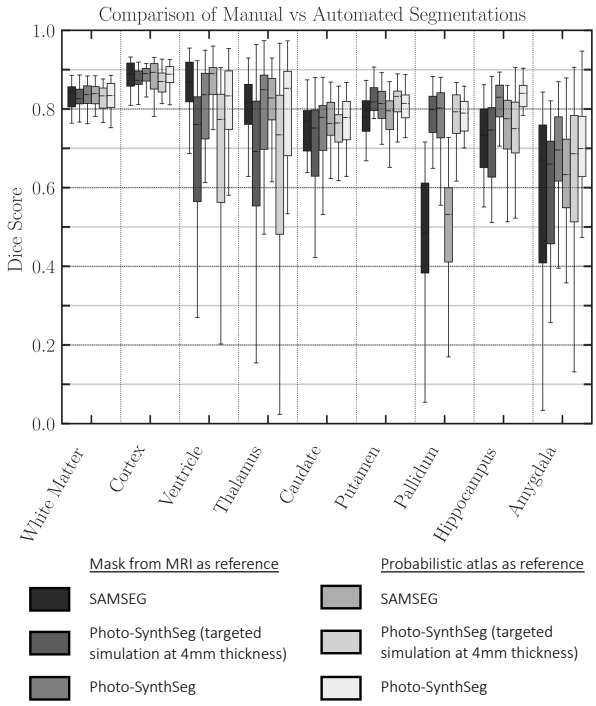

Fig. 12. Dice scores of automated versus manual segmentations on select slices. Box plots for the Dice scores produced by SAMSEG, Photo-SynthSeg, and two ablations (use of probabilistic atlas and targeted simulation with ground truth spacing at 4mm). The Dice scores are computed in 2D, using manual segmentations available on select slices. We also note that the absence of extracerebral tissue in the images contributes to a very high Dice overlap for the cortex.

This evaluation with Dice scores is direct, but: *(i)* is based on a relatively small number of slices, and *(ii)* disregards the ultimate purpose of segmentation, which is downstream analysis in 3D (e.g., volumetry). For this purpose, we also indirectly evaluated the segmentations by analyzing the volumes of brain structures derived from the segmentations of the whole stack. Specifically, we correlated these volumes with silver standard values derived from the isotropic FLAIR MRI scans using "standard" SynthSeg (34). Table 1 shows the correlations (r) and p-values for Steiger tests (p_s) comparing the correlation coefficients achieved by SAMSEG and Photo-SynthSeg – while considering their dependency due to the common ground truth sample. The results show once more that Photo-SynthSeg outperforms SAMSEG for nearly every structure – and in the few cases in which it does not, the Steiger test does not yield a statistically significant difference. We note that the correlations are above 0.8 for most brain structures, indicating that the 3D reconstructed photographs yield usable volumes in volumetric analysis. We also note that the correlations are slightly but consistently lower for the reconstructions with the probabilistic atlas, yielding correlations close to 0.8 for most brain regions.

D. Application to unevenly sliced slabs with real surface scans. In this experiment, we provide results on a dataset from a different biobank (MADRC). These are thick (∼10 mm) slices cut by hand without cutting guides and prioritize cutting on anatomic landmarks over consistent slice thickness. Therefore, this dataset enables us to evaluate our methods in a real world scenario. Moreover, the 3D reference is a real surface scan, rather than a binary mask derived from an MRI.

Since no ground truth is available for this dataset, we evaluated our methods indirectly via a group study of Alzheimer's disease. First, we used the 3D reconstruction method and Photo-SynthSeg to derive the volumes of the different brain regions; since some cases are hemispheres and some cases are full brains, we divide all volumes by two in the latter case. We also note that segmenting single hemispheres required training a specific version of Photo-SynthSeg dedicated to left hemispheres; to process a right hemisphere, we simply flip it, segment it, and flip the results back. Next, we discarded subjects with segmentations not passing a manual quality control performed by JWR and RH. We also discarded cases with frontotemporal dementia, leading to a final sample size $N = 33$. Finally, given the volumes of each structure, we corrected them by sex and age using a general linear model, and compared the values across the two groups using a non-parametric Wilcoxon rank sum test (48), as well as the area under the receiver operating characteristic curve (AUROC), which is the non-parametric equivalent of the effect size.

Figure 13 shows the axial, coronal, and sagittal views of sample reconstruction from a right hemisphere with a surface scan. Our proposed methods successfully generalize to the new dataset, despite the thick slices and different image contrast. Table 2 shows the AUROCs and p-values for the Wilcoxon rank sum test. Our method is able to capture well-known atrophy patterns of Alzheimer's disease, such as hippocampal atrophy and ventricle enlargement.

3. Discussion

Neuroimaging to neuropathology correlation studies explore the relationship between gold-standard pathological diagnoses and imaging phenotypes by transferring the microscopic signatures of pathology to *in vivo* MRI. A significant impediment to this effort is the lack of quantitative tools for *post mortem* tissue analysis. For example, quantitative measurements such as cortical thickness and specific regional atrophy are often estimated qualitatively from 2D coronal slices during gross examination. A solution to this problem is leveraging dissection photography of these coronal slices routinely acquired before histology. By designing algorithms to reconstruct 3D volumes from 2D photographs and subsequently segment them, we have enabled a cost-effective and time-saving link between morphometric phenotypes and neuropathological diagnosis.

Table 1. Correlations of volumes of brains regions estimated by SAMSEG and Photo-SynthSeg from the photographs against the reference values derived from the MRI. The p-values are for Steiger tests comparing the correlations achieved by the two methods (accounting for the common sample).

	Mask from MRI as reference			Probabilistic atlas as reference		
	SAMSEG	Photo-SynthSeg	*p*-value	SAMSEG	Photo-SynthSeg	*p*-value
White Matter	0.935	0.981	0.0011	0.886	0.935	0.0117
Cortex	0.930	0.979	0.0001	0.889	0.920	0.0366
Ventricle	0.968	0.988	0.0004	0.980	0.993	0.0006
Thalamus	0.812	0.824	0.4350	0.812	0.824	0.4252
Caudate	0.719	0.779	0.2525	0.733	0.792	0.2062
Putamen	0.904	0.779	0.9923	0.872	0.792	0.9598
Pallidum	0.727	0.694	0.6171	0.676	0.658	0.5698
Hippocampus	0.830	0.757	0.8873	0.764	0.776	0.4293
Amygdala	0.598	0.703	0.1663	0.576	0.763	0.0221

Our new tools are publicly available and utilize modern deep learning techniques and surface scanning. Being available as part of Freesurfer makes the tools easy to use by anyone with little or no training. Furthermore, the absence of tunable parameters in Photo-SynthSeg makes the results produced by our methods highly reproducible, and the robustness of the tools enables widespread application to heterogeneous datasets. This robustness has been demonstrated by applying the tools to images from two different biobanks, with different slice thickness, tissue processing, and photographic setup.

As mentioned earlier, retrospective reconstruction of datasets (with no accompanying surface scan available) can be achieved with a probabilistic atlas. However, such a reconstruction is laden with ambiguities because the probabilistic atlas does not have access to the true shape of the tissue – which the surface scan directly measures. Whether the increased reconstruction error is tolerable depends on the downstream task, e.g., shape analysis vs volumetry.

While deep learning segmentation tools are increasingly common in medical imaging research, their practical applicability in modalities with highly varying appearance (like dissection photography) has been hindered by their limited generalization ability. Photo-SynthSeg circumvents this problem by building on our recent work on domain randomization (34), and can segment 3D reconstructed stacks of photographs irrespective of the thickness of the slices and of the contrast properties of the tissue. Compared with SAMSEG, Photo-Synthseg also has the advantage of estimating the segmentation between slices (Section C). Moreover, Photo-Synthseg inherits the computational efficiency of neural networks, and can segment a whole case in a few seconds (or tens of seconds if no GPU is available) without any special requirements on machine learning expertise – thus enabling broad applicability.

While registration and segmentation enable morphometry and neuropathology-neuroimaging correlation, accurate white matter and pial surface placement on 3D reconstructed photographs are crucial for enhanced cortical analyses. In the future, we hope to extend Photo-SynthSeg to enable surface fitting for cortical placement and parcellation. While the convoluted nature of cortical surfaces makes this task difficult for photograph volumes, integrating the triangular mesh provided by the surface scanner could enable accurate surface placement. Additional future analyses will include: correlating the segmentation-derived volumes with clinical scores, disease subtypes, and disease duration; and using techniques like SynthSR (49) to improve the resolution of the reconstructed volumes.

4. Conclusion

Leveraging the vast amounts of dissection photographs available at brain banks worldwide to perform morphometry is a promising avenue for enhancing our understanding of various neurodegenerative diseases. Our new tools will allow extraction of quantitative phenotypical information from these photographs – and thus augmentation of histopathological analysis. We expect this new methodology to play a crucial role in the discovery of new imaging markers to study neurodegenerative diseases.

ACKNOWLEDGMENTS. This research was supported by primarily supported by the National Institute of Aging (R01AG070988 and P30AG062421). Other support was provided by NIH grants RF1MH123195, R01EB031114, UM1MH130981, K08AG065426, P30AG066509, U19AG066567, R01NS112161; the European Union (ERC Starting Grant 677697); Alzheimer's Research UK (ARUK-IRG2019A-003); and the Massachusetts Life Sciences Center. AC was further funded by the European Union, the Ministry of Universities and Recovery, and the Transformation and Resilience Plan, through a call from Universitat Politècnica de Catalunya (Grant Ref. 2021UPC-MS-67573). Additional support was provided by NIH grants U01MH117023, 1R01EB023281, R01EB006758, R21EB018907, R01EB019956, P41EB030006, 1R56AG064027, 1R01AG064027, 5R01AG008122, R01AG016495, 1R01AG070988,

Table 2. Area under the receiver operating characteristic curve (AUROC) and p-value of a non-parametric Wilcoxon rank sum test comparing the volumes of brain regions for Alzheimer's cases vs controls. The volumes were corrected by age and sex using a general linear model. We note that the AUROC is bounded between 0 and 1 (0.5 is chance) and is the non-parametric equivalent of the effect size (higher AUROC corresponds to larger differences). The sample size is $N = 33$.

Region	Wh Matter	Cortex	Vent	Thal	Caud	Putamen	Pallidum	Hippoc	Amyg
AUROC	.45	.52	.73	.48	.65	.64	.77	.75	. 77
p-value	.666	.418	.016	.596	.0863	.092	.005	.009	.007

DRAFT

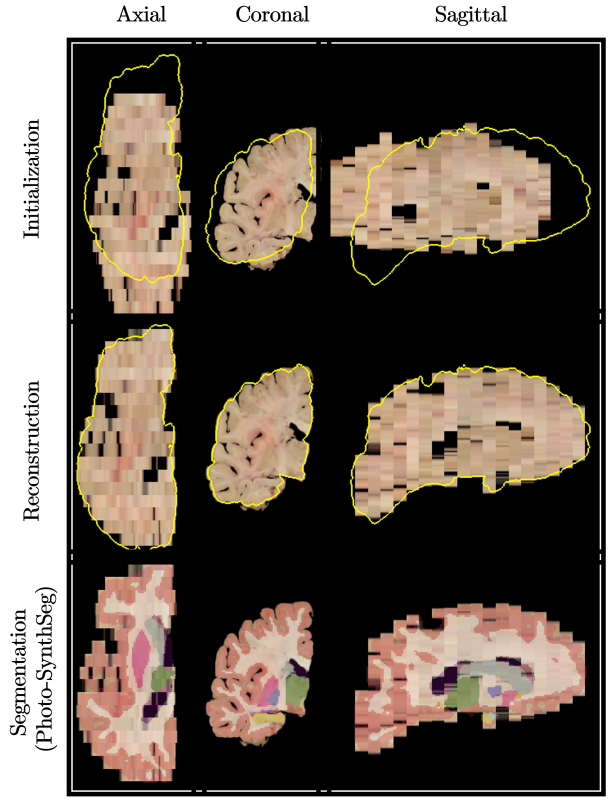

Fig. 13. Reconstruction and segmentation of thick slices from the MADRC dataset. Axial, Coronal, and Sagittal views of a sample case (right hemisphere) before and after reconstruction and of the corresponding automated segmentation using Photo-SynthSeg.

UM1MH130981, R01 MH123195, R01 MH121885, 1RF1MH123195, R01NS0525851, R21NS072652, R01NS070963, R01NS083534, 5U01NS086625,5U24NS10059103, R01NS105820, 1S10RR023401, 1S10RR019307, 1S10RR023043, and 5U01MH093765.

Bibliography

1. DH Salat, et al., Thinning of the cerebral cortex in aging. *Cereb. cortex* **14**, 721–730 (2004).
2. KB Walhovd, et al., Effects of age on volumes of cortex, white matter and subcortical structures. *Neurobiol. aging* **26**, 1261–1270 (2005).
3. P Coupé, G Catheline, E Lanuza, JV Manjón, ADN Initiative, Towards a unified analysis of brain maturation and aging across the entire lifespan: A MRI analysis. *Hum. brain mapping* **38**, 5501–5518 (2017).
4. JP Lerch, et al., Focal decline of cortical thickness in alzheimer's disease identified by computational neuroanatomy. *Cereb. cortex* **15**, 995–1001 (2005).
5. RS Desikan, et al., Automated MRI measures identify individuals with mild cognitive impairment and alzheimer's disease. *Brain* **132**, 2048–2057 (2009).
6. BC Dickerson, et al., Differential effects of aging and alzheimer's disease on medial temporal lobe cortical thickness and surface area. *Neurobiol. aging* **30**, 432–440 (2009).
7. AE Blanken, et al., Associations between hippocampal morphometry and neuropathologic markers of alzheimer's disease using 7T MRI. *NeuroImage: Clin.* **15**, 56–61 (2017).
8. JM Webster, et al., Leveraging Neuroimaging Tools to Assess Precision and Accuracy in an Alzheimer's Disease Neuropathologic Sampling Protocol. *Front. Neurosci.* **15** (2021).
9. BL Edlow, et al., 7 tesla mri of the ex vivo human brain at 100 micron resolution. *Sci. data* **6**, 1–10 (2019).
10. AS Shatil, KM Matsuda, CR Figley, A method for whole brain ex vivo magnetic resonance imaging with minimal susceptibility artifacts. *Front. neurology* **7**, 208 (2016).
11. R Ravid, Biobanks for biomarkers in neurological disorders: the Da Vinci bridge for optimal clinico-pathological connection. *J. Neurol. Sci.* **283**, 119–126 (2009).
12. S Love, Neuropathological investigation of dementia: a guide for neurologists. *J. Neurol. Neurosurg. & Psychiatry* **76**, v8–v14 (2005).
13. I Goodfellow, Y Bengio, A Courville, *Deep learning.* (MIT press), (2016).
14. J Salvi, J Pages, J Batlle, Pattern codification strategies in structured light systems. *Pattern recognition* **37**, 827–849 (2004).
15. O Ronneberger, P Fischer, T Brox, U-Net: Convolutional Networks for Biomedical Image Segmentation in *Medical Image Computing and Computer-Assisted Intervention – MICCAI 2015*, Lecture Notes in Computer Science, eds. N Navab, J Hornegger, WM Wells, AF Frangi. (Springer International Publishing, Cham), pp. 234–241 (2015).
16. B Billot, et al., SynthSeg: Domain Randomisation for Segmentation of Brain Scans of any Contrast and Resolution. *arXiv:2107.09559 [cs, eess]* (2021) arXiv: 2107.09559.
17. HF Tregidgo, et al., 3d reconstruction and segmentation of dissection photographs for mri-free neuropathology in *Medical Image Computing and Computer Assisted Intervention–MICCAI 2020: 23rd International Conference, Lima, Peru, October 4–8, 2020, Proceedings, Part V 23.* (Springer), pp. 204–214 (2020).
18. DG Lowe, Object recognition from local scale-invariant features in *Proceedings of the seventh IEEE international conference on computer vision.* (Ieee), Vol. 2, pp. 1150–1157 (1999).
19. JA Maintz, MA Viergever, A survey of medical image registration. *Med. image analysis* **2**, 1–36 (1998).
20. JP Pluim, JA Maintz, MA Viergever, Mutual-information-based registration of medical images: a survey. *IEEE transactions on medical imaging* **22**, 986–1004 (2003).
21. B Zitova, J Flusser, Image registration methods: a survey. *Image vision computing* **21**, 977–1000 (2003).
22. A Sotiras, C Davatzikos, N Paragios, Deformable medical image registration: A survey. *IEEE transactions on medical imaging* **32**, 1153–1190 (2013).
23. J Pichat, JE Iglesias, T Yousry, S Ourselin, M Modat, A survey of methods for 3d histology reconstruction. *Med. image analysis* **46**, 73–105 (2018).
24. M Mancini, et al., Hierarchical joint registration of tissue blocks with soft shape constraints for large-scale histology of the human brain in *2019 IEEE 16th International Symposium on Biomedical Imaging (ISBI 2019).* (IEEE), pp. 666–669 (2019).
25. DW Shattuck, et al., Construction of a 3d probabilistic atlas of human cortical structures. *Neuroimage* **39**, 1064–1080 (2008).
26. LR Dice, Measures of the amount of ecologic association between species. *Ecology* **26**, 297–302 (1945).
27. TA Sorensen, A method of establishing groups of equal amplitude in plant sociology based on similarity of species content and its application to analyses of the vegetation on danish commons. *Biol. Skar.* **5**, 1–34 (1948).
28. F Milletari, N Navab, SA Ahmadi, V-net: Fully convolutional neural networks for volumetric medical image segmentation in *2016 fourth international conference on 3D vision (3DV).* (Ieee), pp. 565–571 (2016).
29. R Fletcher, Practical methods of optimization john wiley & sons. *New York* **80** (1987).
30. DL Pham, C Xu, JL Prince, Current methods in medical image segmentation. *Annu. review biomedical engineering* **2**, 315–337 (2000).
31. I Despotović, B Goossens, W Philips, MRI segmentation of the human brain: challenges, methods, and applications. *Comput. mathematical methods medicine* **2015** (2015).
32. Z Akkus, A Galimzianova, A Hoogi, DL Rubin, BJ Erickson, Deep learning for brain MRI segmentation: state of the art and future directions. *J. digital imaging* **30**, 449–459 (2017).
33. J Tobin, et al., Domain randomization for transferring deep neural networks from simulation to the real world in *2017 IEEE/RSJ international conference on intelligent robots and systems (IROS).* (IEEE), pp. 23–30 (2017).
34. B Billot, et al., Synthseg: Segmentation of brain MRI scans of any contrast and resolution without retraining. *Med. Image Analysis* p. 102789 (2023).
35. B Billot, et al., Robust machine learning segmentation for large-scale analysis of heterogeneous clinical brain MRI datasets. *Proc. Natl. Acad. Sci.* **120**, e2216399120 (2023).
36. Ö Çiçek, A Abdulkadir, SS Lienkamp, T Brox, O Ronneberger, 3d u-net: learning dense volumetric segmentation from sparse annotation in *Medical Image Computing and Computer-Assisted Intervention–MICCAI 2016: 19th International Conference, Athens, Greece, October 17-21, 2016, Proceedings, Part II 19.* (Springer), pp. 424–432 (2016).
37. B Billot, et al., A Learning Strategy for Contrast-agnostic MRI Segmentation in *Medical Imaging with Deep Learning.* pp. 75–93 (2020).
38. S Ioffe, C Szegedy, Batch Normalization: Accelerating Deep Network Training by Reducing Internal Covariate Shift in *International Conference on Machine Learning.* pp. 448–456 (2015).
39. DA Clevert, T Unterthiner, S Hochreiter, Fast and Accurate Deep Network Learning by Exponential Linear Units (ELUs). *arXiv:1511.07289 [cs]* (2016).
40. DP Kingma, J Ba, Adam: A method for stochastic optimization. *arXiv preprint arXiv:1412.6980* (2014).
41. F Chollet, Keras (2015) https://keras.io.
42. M Abadi, P Barham, J Chen, Z Chen, A Davis, Tensorflow: A system for large-scale machine learning in *Symposium on Operating Systems Design and Implementation.* pp. 265–283 (2016).
43. B Fischl, et al., Whole brain segmentation: automated labeling of neuroanatomical structures in the human brain. *Neuron* **33**, 341–355 (2002).
44. B Fischl, Freesurfer. *Neuroimage* **62**, 774–781 (2012).
45. DC Van Essen, et al., The human connectome project: a data acquisition perspective. *Neuroimage* **62**, 2222–2231 (2012).
46. CS Latimer, et al., Protocol for the systematic fixation, circuit-based sampling, and qualitative and quantitative neuropathological analysis of human brain tissue in *Alzheimer's Disease.* (Springer), pp. 3–30 (2023).
47. O Puonti, JE Iglesias, K Van Leemput, Fast and sequence-adaptive whole-brain segmentation using parametric bayesian modeling. *NeuroImage* **143**, 235–249 (2016).
48. HB Mann, DR Whitney, On a test of whether one of two random variables is stochastically larger than the other. *The annals mathematical statistics* pp. 50–60 (1947).
49. JE Iglesias, et al., Synthsr: A public ai tool to turn heterogeneous clinical brain scans into high-resolution t1-weighted images for 3d morphometry. *Sci. advances* **9**, eadd3607 (2023).

DRAFT

Appendix

A. Data Acquisition

A. Alzheimer's Disease Research Center, University of Washington (UW-ADRC). The whole brain is removed using standard autopsy procedures. The brain is weighed and photo-documented, and then the meninges are removed. For donors with a postmortem interval (PMI: the time interval between death and procurement) longer than 12 hours, the whole brain is fixed in 10% *Neutral-buffered formalin* (NBF) with no tissue frozen. A rapid slicing protocol is performed for donors with a post-mortem interval of fewer than 12 hours. For a rapid protocol, the brain is bisected along the midline, and one hemibrain is placed in a bucket with 10% NBF for two weeks. The other hemibrain is 3D surface scanned, then placed in a scaffolding box with the vermis of the cerebellum flush against the posterior wall. The hemibrain is embedded in freshly mixed dental alginate (540g powder blended in 4L of water) and submerged until the alginate is set. The alginate block containing the hemibrain is placed in a slicing sled with the frontal pole toward the front. The hemibrain is sliced anterior to posterior in 4mm slices. All slices are set on Teflon-coated aluminum plates and photographed. Alternating slices are set to be flash-frozen, with the remaining slices fixed in 10% NBF. The hemibrain (rapid) or whole (non-rapid) brain is fixed in 10% NBF for two weeks, embedded in agarose, and scanned in a 3T MRI scanner.

Following the MRI, the agarose-embedded brain is sliced on a modified deli slicer for precise 4 mm tissue slabs aligned with the ex vivo MRI images for image-guided tissue sampling to standard tissue sampling following the current National Institute of Aging-Alzheimer's Association (NIA-AA) consensus guidelines. After sampling, all blocks are processed and embedded in paraffin according to standard techniques. Following current NIA-AA guidelines, the resulting Fast-Frozen Paraffin-Embedded (FFPE) blocks are cut and stained for diagnostic analysis. Histologically stained slides are scanned into the HALO (https://indicalab.com/halo/) imaging workstation using an Aperio AT2 slide scanner and are analyzed by a trained neuropathologist.

B. Massachusetts Alzheimer's Disease Research Center (MADRC). The whole brain is removed using standard autopsy procedures. After removal of the dura matter, the brain is weighed, photo-documented, and then fixed in 10% neutral-buffered formalin. Some specimens are cut along the midline sagittal plane with one hemibrain frozen for future biochemical studies. After at least one week of fixation, the specimens are photo-documented again. The posterior fossa is then dissected off the fixed full or hemibrain through the midbrain at the level of cranial nerve III, and the supratentorial portion of the brain is 3D surface scanned.

After scanning, the brain or hemibrain is sectioned at defined anatomical landmarks (anterior temporal tips, optic chiasm, infundibulum, mamillary bodies, cerebral peduncles, red nuclei, and colliculi) with the frontal and occipital lobes additionally sectioned at approximately 10 mm intervals. The front and back of all sections are then photographed with a metric ruler included for size reference. The photographs are then deidentified for further analysis.

DRAFT

Supplementary Material

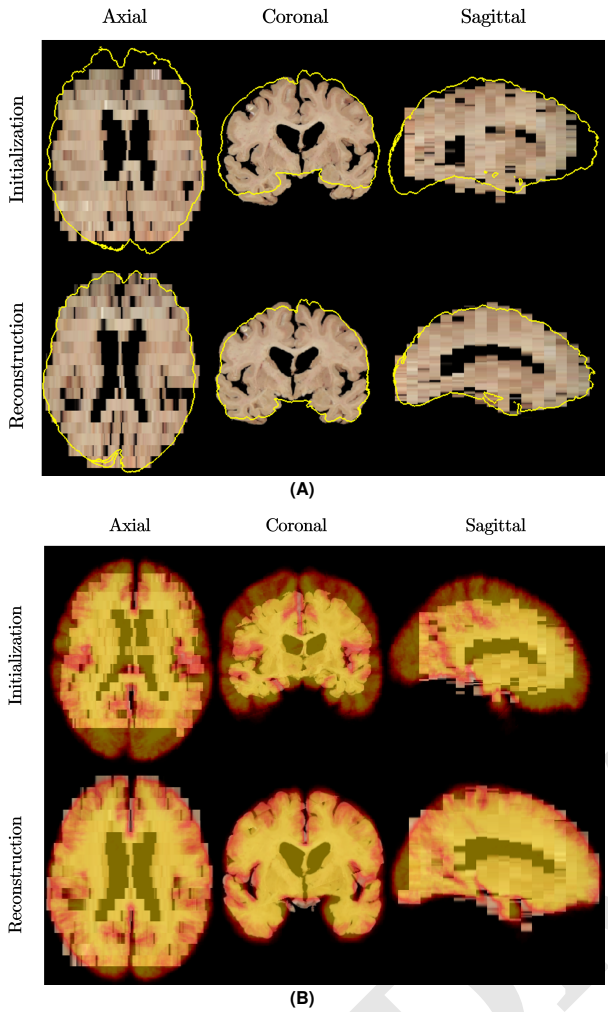

Fig. S1. 3D volumetric reconstruction of dissection photographs of a case from the MADRC dataset. (A) Axial, coronal, and sagittal views of the photograph stack at initialization and after reconstruction with a surface scan reference (overlaid as a yellow line). **(B)** The three views at initialization and after reconstruction with a probabilistic atlas (overlaid as a heat map).

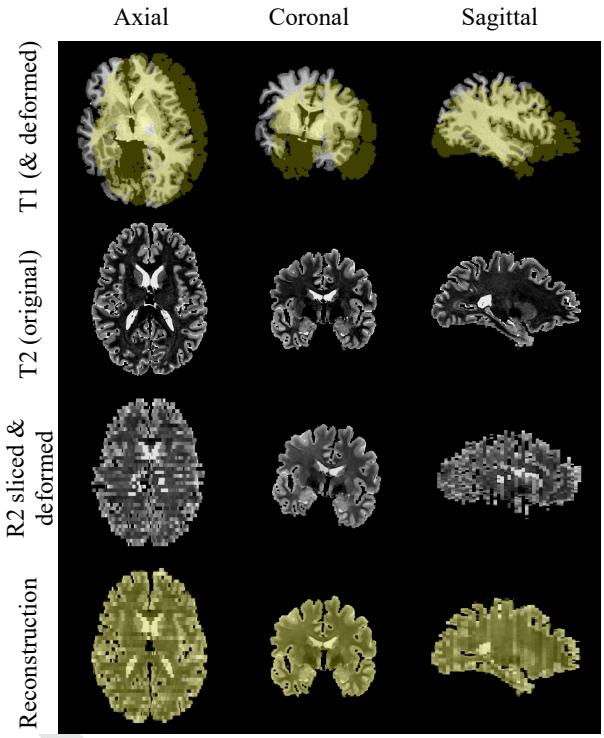

Fig. S2. Simulation and reconstruction of synthetic data. Top row: skull stripped T1 scan and (randomly translated and rotated) binary mask of the cerebrum, in yellow. Second row: original T2 scan. Third row: randomly sliced and linearly deformed T2 images. Bottom row: output of the 3D reconstruction algorithm, i.e., reconstructed T2 slices and registered reference mask overlaid in yellow.